

Trade-off between angular resolution and straylight contamination in CMB anisotropy experiments.

II. Straylight evaluation.

C. Burigana¹, M. Sandri¹, F. Villa¹, D. Maino², R. Paladini³, C. Baccigalupi³,
M. Bersanelli², and N. Mandolesi¹

¹ IASF/CNR, Sezione di Bologna, via P. Gobetti, 101, I-40129 Bologna, Italy
e-mail: burigana, sandri, villa, mandolesi @bo.iasf.cnr.it

² Dipartimento di Fisica, Università degli Studi di Milano, via Celoria, 16, I-20133
Milano, Italy
e-mail: bersanelli, maino @uni.mi.astro.it

³ SISSA, International School for Advanced Studies, via Beirut, 2-4, I-34014
Trieste, Italy
e-mail: paladini, bacci @sisssa.it

On behalf of the LFI Consortium

Sent March 27, 2003

Abstract. Satellite CMB anisotropy missions, such as WMAP and PLANCK, and also the new generation of balloon-borne and ground experiments, make use of complex multi-frequency instruments at the focus of a meter class telescope to allow the joint study of CMB and foreground anisotropies, necessary for a high quality component separation. Between ~ 70 GHz and ~ 300 GHz, where foreground contamination is minimum, it is extremely important to reach the best trade-off between the improvement of the angular resolution, necessary to measure the high order acoustic peaks of CMB anisotropy, and the minimization of the straylight contamination mainly due to the Galactic emission. This is one of the most critical systematic effects at large and intermediate angular scales (i.e. at multipoles ℓ less than ≈ 100) and consists in unwanted radiation entering the beam at large angles from the direction of the antenna boresight direction. We focus here, as a working case, on the 30 and 100 GHz channels of the PLANCK Low Frequency Instrument (LFI). By assuming the nominal PLANCK scanning strat-

egy, we evaluate the GSC introduced by the most relevant Galactic foreground components for a reference set of optical configurations, accurately simulated as described in Paper I. We show that it is possible to improve the angular resolution of 5 – 7 % by keeping the overall peak-to-peak GSC below the level of few μK (and about 10 times smaller in terms of RMS). A comparison between the level of straylight introduced by the different Galactic components for different beam regions (intermediate and far sidelobes) is presented. Simple approximate relations giving the RMS and peak-to-peak levels of the GSC for the intermediate pattern and far sidelobes as functions of the corresponding contributions to the integrated antenna pattern are provided. We compare the results obtained at 100 GHz with those at 30 GHz, where GSC is more critical. Finally, for some reference cases we compare the results based on Galactic foreground templates derived from radio and IR surveys with those based on WMAP maps including CMB and extragalactic source fluctuations.

Key words. Cosmology: cosmic microwave background – Galaxy: general – Space vehicles – Telescopes – Methods: data analysis.

1. Introduction

After the detection of cosmic microwave background (CMB) anisotropies at few degree scales by COBE/DMR (Smoot et al. 1992, Bennett et al. 1996, Górski et al. 1996) and the recent balloon-borne and ground experiments (see Bersanelli et al. 2002 and references therein for a review on the pre-WMAP observational status) at high sensitivity and resolution on limited sky regions probing a universe model with $\Omega_{tot} \sim 1$ (see e.g. Netterfield et al. 2002, Stompor et al. 2001, Pryke et al. 2002, and references therein) the NASA space mission WMAP (Wilkinson Microwave Anisotropy Probe, see Bennett et al. 2003a) derived the CMB anisotropy angular power spectrum with unprecedented sensitivity and reliability (Hinshaw et al. 2003b, Kogut et al. 2003) and improved the accuracy in the determination of the most important cosmological parameters (Spergel et al. 2003).

Future fundamental progresses in CMB anisotropy and polarization will be based on the PLANCK mission by ESA ¹ (Bersanelli et al. 1996, Tauber 2000, Villa et al. 2003), planned to be launched in the year 2007.

In particular, the Low Frequency Instrument (LFI, Mandolesi et al. 1998; see also Mandolesi et al. 2002) and the High Frequency Instrument (HFI, Puget et al. 1998; see also Lamarre et al. 2002) on-board PLANCK will cover together a wide frequency range (30–900 GHz) which should significantly improve the accuracy of the subtraction of foreground contamination from the primordial CMB anisotropy, providing at the same

Send offprint requests to: C. Burigana

¹ <http://astro.estec.esa.nl/Planck/>

time a gold mine of cosmological as well as astrophysical information (see e.g. De Zotti et al. 1999 and references therein).

To fully reach these scientific goals, great attention has to be devoted to properly reduce and/or subtract all the possible systematic effects.

The effect of optical distortions, both in the main beam and in the near and far sidelobes, has been widely recognized as one of the most critical systematics both in balloon experiments and in space missions (Page et al. 2003, Barnes et al. 2003).

The systematic effect introduced by main beam distortions (Burigana et al. 1998) can be in part reduced by adopting aplanatic configurations for the primary mirror (Villa et al. 1998, Mandolesi et al. 2000a, Villa et al. 2002) and its effect on the CMB anisotropy power spectrum recovery, relevant at the multipoles of the acoustic peaks, can be partially removed through dedicated deconvolution codes (Arnau et al. 2002) provided that the main beam shape can be accurately reconstructed in flight (Burigana et al. 2002).

The requirement on the rejection of unwanted radiation coming from directions far from the optical axis (straylight) is stringent for PLANCK and does not pertain only the telescope itself, but the entire optical system, including solar panels, shielding, thermal stability and focal assembly components. The variations of the spurious straylight signal introduce contaminations in the anisotropy measurements. The removal of this effect in data analysis is in principle much more complicated than the subtraction of main beam distortion effect. This is due to the difficulty to accurately known the “real” antenna pattern (with both at ground and in flight reconstruction) at very low response levels.

The antenna response features far from the beam centre (sidelobes) are determined largely by diffraction and scattering from the edges of the mirrors and from nearby supporting structures. Therefore, they can be reduced by decreasing the illumination at the edge of the primary, i.e. increasing the edge taper (ET if expressed in dB; the linear edge taper, LET, is $10^{-ET/10}$), defined as the ratio of the power per unit area incident on the centre of the mirror to that incident on the edge. Of course, the higher is edge taper, the lower is the sidelobe level and the straylight contamination. On the other hand, increasing the edge taper has a negative impact on the angular resolution for a fixed size of the primary mirror (see e.g. Mandolesi et al. 2000b).

In the “cosmological window” between ~ 70 GHz and ~ 300 GHz, where foreground contamination is minimum, it is extremely important to reach the best trade-off between the improvement of the angular resolution, necessary to measure the high order acoustic peaks of CMB anisotropy, and the minimization of the straylight contamination due to the Galactic emission (GSC, Galaxy Straylight Contamination), one of the most critical systematic effects, most relevant at large and intermediate angular scales (i.e. at multipoles ℓ less than ≈ 100).

In this work we focus, as a working case, on the 100 GHz channels of PLANCK Low Frequency Instrument, although the methods and the basic results described here can

Please give a shorter version with: `\authorrunning` and/or `\titilerunning` prior to `\maketitle`

be applied also to other PLANCK frequency channels and to different CMB anisotropy experiments. We shall also compare our results with simulated data at 30 GHz.

We will use here the detailed analysis on optical computations and the main optical results concerning the full antenna pattern response given in Sandri et al. 2003 (hereafter Paper I). We present extensive simulations of the GSC due to Galactic foreground components relevant at 100 GHz and, at this purpose, we have made use of a wide set of simulated optical configurations in order to find the best compromise between resolution and GSC therefore defining the maximum range of multipoles accessible to the considered frequency channel and the level of straylight signal affecting the data.

In Sect. 2 we briefly describe the basic recipes to simulate PLANCK observations (see also Appendix A), the adopted optical input, and maps of Galactic components. The results of the simulated straylight contamination are described in Sect. 3, while the comparison between the results obtained for different antenna patterns and foreground components is presented in Sect. 4 (and in Appendix B for the comparison with a straylight simulation at 30 GHz). Finally, we discuss the results and draw our main conclusions in Sect. 5.

2. Simulations

The selected orbit for PLANCK is a Lissajous orbit around the Lagrangian point L2 of the Sun-Earth system (see e.g. Mandolesi et al. 1998). The spacecraft spins at 1 r.p.m. and the field of view of the two instruments (LFI/HFI) is about $10^\circ \times 10^\circ$ centered at the telescope optical axis (the so-called telescope line of sight, LOS) at a given angle α from the spin-axis direction, given by a unit vector, \mathbf{s} , chosen to be pointed in the opposite direction with respect to the Sun. In this work we consider values of $\alpha \sim 85^\circ$, as adopted for the baseline scanning strategy. The spin axis will be kept parallel to the Sun-spacecraft direction and reoriented by $\simeq 2.5'$ every $\simeq 1$ hour (baseline scanning strategy). Hence PLANCK will trace large circles in the sky. A precession of the spin-axis with a period, P , of $\simeq 6$ months at a given angle $\beta \sim 10^\circ$ about an axis, \mathbf{f} , parallel to the Sun-spacecraft direction (and outward the Sun) and shifted of $\simeq 2.5'$ every $\simeq 1$ hour, may be included in the scanning strategy, possibly with a modulation of the speed of the precession in order to optimize data transmission (Bernard et al. 2002). Although the scanning strategy could be changed, the GSC pattern, peak-to-peak, and angular power spectrum are very weakly dependent on the details of these proposed scanning strategies (Burigana et al. 2000).

The code we have implemented for simulating PLANCK observations for a wide set of scanning strategies is described in detail in Burigana et al. (1997, 1998) and in Maino et al. (1999). In this study we exploit the baseline scanning strategy and simply assume

PLANCK located in L2. We do not consider the PLANCK Lissajous orbit around L2 because its effects are negligible in this context.

We compute the convolutions between the antenna pattern response and the sky signal as described in Burigana et al. (2001) by working at $\sim 1^\circ$ or $\sim 7'$ resolution when considering the far or the intermediate sidelobes and by considering spin-axis shifts of $\sim 2^\circ$ every two days and 180 samplings per scan circle. In fact, the effects of pattern features we want to study here occur at \sim degree or larger scales and, also, the wide set of optical simulations for the full antenna pattern is available at \sim degree resolution (see Paper I for details on computation time of optical simulations).

With respect to the reference frames described in Burigana et al. (2001), following the recent developments in optimizing the polarization properties of LFI main beams (see Paper I), the conversion between the standard Cartesian *telescope frame* x, y, z and the *beam frame* x_{bf}, y_{bf}, z_{bf} requires a further angle ψ_B other than the standard polar coordinates θ_B and ϕ_B defining the colatitude and the longitude of the main beam centre direction in the *telescope frame*. Appendix A provides the transformation rules between the *telescope frame* and the *beam frame*, as well as the definition of the reference frames adopted in this work.

The orientation of these frames as the satellite moves is implemented in the code. For each integration time, we determine the orientations in the sky of the *telescope frame* and of the *beam frame*, thus performing a direct convolution between the full pattern response and the sky signal for the desired number of maps, simultaneously.

2.1. Optical inputs

A detailed discussion of the optical simulation method and results is presented in Paper I (see Tables 2 and 3 of Paper I for the main properties of the adopted antenna patterns). We briefly summarize here the most relevant aspect in this context.

Several full beam patterns have been simulated for different designs of two PLANCK LFI feedhorns at 100 GHz differently located on the focal plane unit: three models (9A, 9B, 9C) for LFI9 and four models (4A, 4B, 4C, 4D) for LFI4. Different values of ET will reflect in significant differences in the level of the GSC in the TOD, while different feed designs with the same ET will produce small, but not negligible, differences.

The details of the antenna pattern response, computed as described in Paper I as functions of the two standard polar coordinates θ_{bf}, ϕ_{bf} in the *beam frame*, depend also on the optical contributions considered in the analysis. For some representative cases, we will compare the results of our simulations of GSC by adopting optical computations taking into account the first and second or the first, second and third order optical interactions (see Paper I).

In the *beam frame* we identify two different angular regions relevant for the straylight analysis: the intermediate pattern and the far sidelobes, respectively defined as the region between 1.2° and 5° from the beam centre direction and at angles large than 5° from the beam centre direction. The definition of these “reference” angles is, of course, somewhat arbitrary. They roughly separate angular regions where significant pattern variations occur on sub-degree scales from those where they occur on scales of few degrees or larger. The values adopted here allow a direct comparison with a previous analysis (Burigana et al. 2001).

2.2. Maps of Galactic components

In the cosmological window (70–300 GHz) the CMB is clearly the dominant component; on the other hand the Galactic emission is still relevant at low and middle Galactic latitudes. The templates adopted here are similar to those described in Maino et al. (2002) and Paladini et al. (2003).

At 100 GHz the most relevant Galactic component is the thermal dust emission. We adopted here a template obtained by extrapolating the maps by Schlegel et al. (1998) which combines IRAS and DIRBE data, assuming a grey-body spectrum (expressed in antenna temperature),

$$T_{A,dust}(\nu) \propto \frac{\tilde{\nu}^{\beta+1}}{e^{\tilde{\nu}} - 1}, \quad \tilde{\nu} = \frac{h\nu}{kT_{dust}} \quad (1)$$

with uniform temperature $T_{dust} = 18$ K and emissivity $\beta = 2$.

In order to simulate the free-free contribution we assume, somewhat arbitrarily, that it is perfectly correlated with the dust itself, i.e. that it has the same spatial distribution. Its antenna temperature scales with frequency as $T_{A,ff} \propto \nu^{-\beta_{ff}}$, with $\beta_{ff} = -2.1$. The relative amplitude of dust and free-free emission is assumed to be a factor of 3 at 100 GHz (De Zotti et al. 1999). Thus, we produce a single map of “thermal” emission from dust plus diffuse free-free emission (see Fig. 1) with a spectrum described by:

$$T_{A,thermal}(\nu) = \left[\frac{1}{3} \left(\frac{\nu}{100\text{GHz}} \right)^{\beta_{ff}} + \frac{T_{A,dust}(\nu)}{T_{A,dust}(100\text{GHz})} \right] \times T_{A,dust}(100\text{GHz}). \quad (2)$$

The synchrotron emission template is the 408 MHz map of Haslam et al. (1982), available at a resolution of 0.85° , extrapolated to the considered frequencies (see Fig. 2) assuming a uniform spectral index $\beta_{syn} = -2.9$ in antenna temperature. No attempt is made here to add small scale fluctuations, since the effects of pattern features on which this work is focused occur at \sim degree or larger scales; for the same reason, the fact the original template includes a convolution with a beam with the given resolution is not a concern.

Localized free-free emission dominates the signal on wide areas in the Galactic plane at least over the frequency range from 30 to 100 GHz. The Synthetic Catalog at 2.7 GHz produced by Paladini et al. (2003) provides a rich information on compact Galactic HII

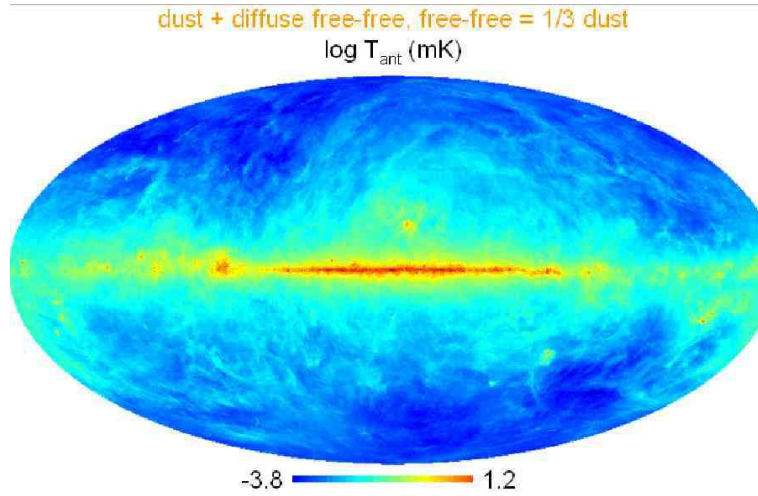


Fig. 1. Map of the Galactic dust emission plus diffuse free-free emission adopted in this study (see also the text).

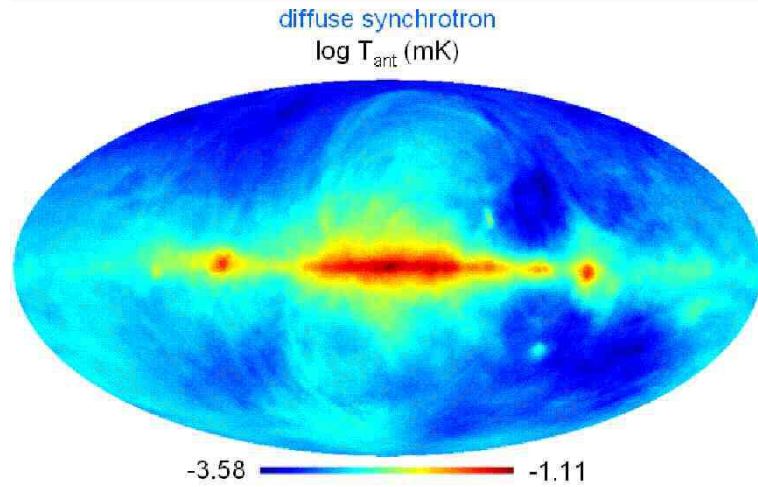


Fig. 2. Map of the Galactic diffuse synchrotron emission adopted in this study (see also the text).

regions that has been used in this work to generate a map of free-free emission from these sources (see Fig. 3). A spectral index $\alpha = -0.1$ in flux (-2.1 in antenna temperature), as in the case of thermal bremsstrahlung emission in a thin plasma, has been adopted here to extrapolate the signal from 2.7 GHz to the considered PLANCK frequency channels. With respect to the simulated map reported by Paladini et al. (2003), we have implemented here a code which simulates the contribution of each source in the Synthetic Catalog to each map pixel without applying at this step the convolution with the beam, since the convolution with the intermediate and far antenna pattern has been subsequently applied as described in the first part of this section.

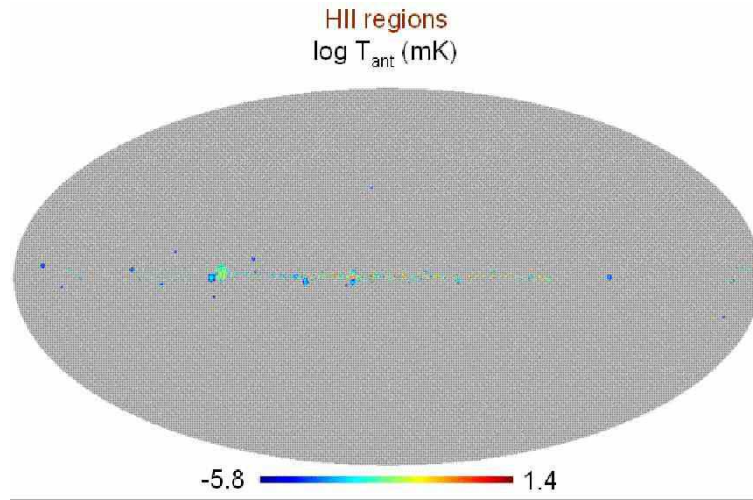


Fig. 3. Map of the free-free emission from compact Galactic HII regions adopted in this study (see also the text).

All maps have been projected into the HEALPix scheme ² (*Hierarchical Equal Area and IsoLatitude Pixelization of the Sphere*) by Górski et al. (1999).

While this work was nearly completed, the 1 year data products ³ from the WMAP satellite have become available. In a few representative cases, we have repeated the straylight analysis by adopting the WMAP frequency maps at 33 and 94 GHz, including in the straylight evaluation also the minor contributions to straylight signal from CMB and extragalactic source fluctuations ⁴. Note that WMAP maps are, of course, convolved with the corresponding beam patterns and include the effect of main beam distortions and straylight contamination as well as the instrumental noise and the effect of other systematics not subtracted in the data analysis; on the other hand, these effects are significantly smaller than the signal (Hinshaw et al. 2003a) and, since this analysis is mainly contributed by signal variations on degree or larger angular scales, they can be neglected.

3. Simulation results

The main output of our simulation code are the time ordered data (TOD) of the signals entering the intermediate and far pattern.

In the TOD of each scan circle, two prominent maxima typically appear. These are related, for the intermediate pattern, to the two crossings of the Galactic plane of the telescope field of view and to the crossings of the Galactic plane of the main spillover

² <http://www.eso.org/science/healpix/>

³ <http://lambda.gsfc.nasa.gov>

⁴ Note that these WMAP maps do not include the monopole, while our Galactic component maps include the corresponding monopoles. The comparison between the average straylight signals will be therefore only indicative. Clearly, anisotropy experiments are not sensitive to the monopole, directly subtracted in the data.

in the case of the far pattern. As already recognized by Burigana et al. (2001), these maxima are only slightly shifted with respect to the maxima of the signal entering the main beam in the case of the intermediate pattern and shifted of about 90° in the case of the far pattern, as direct consequence of the pattern shape.

The typical signal level is determined by the sky signal and the fraction, $f_{\%} = 100 \int_{\underline{\Omega}} Jd\Omega / \int_{4\pi} Jd\Omega$, of integrated antenna response in the considered antenna pattern region, $\underline{\Omega}$, reported in Table 3 of Paper I. The ratio between the fraction of the integrated antenna response in the far pattern and the one in the intermediate pattern provides only a rough upper limit to the ratio of straylight peak-to-peak signal in these two pattern regions. In fact, while an extended very bright Galactic region could quite easily fill the (relatively small) solid angle subtended by the intermediate pattern, the whole (quite large) solid angle subtended by the main spillover and by the other relevant far pattern features can not be easily filled by signals coming all simultaneously from very bright Galactic regions. Similarly, the fractional difference between the integrated antenna response in the far pattern computed by including or not the third order optical interaction provides an upper limit (less than about 10%) to the fractional underestimation of the GSC when the third order optical interaction is neglected. More accurate estimates require numerical simulations.

In Figs. 4 and 5 we report the TOD corresponding to the straylight signal respectively from the far and intermediate pattern for the three Galactic components described in Sect. 2.2 in the case of the beam LFI9 9B computed by including the first, second and third order optical interactions.

The TOD corresponding to the difference between the straylight signal obtained by including or neglecting the third order optical interaction are reported in Figs. 6 and 7. Clearly, the difference is within $\sim 5\%$ of the straylight signal, i.e. smaller than the above upper limit derived on the basis of simple optical considerations by about a factor two. Therefore, considering only the first and second order optical interactions does not introduce relevant loss of information in the optimization analysis of the optical design ⁵.

By comparing Figs. 1, 2, and 3 with Figs. 4 and 5, note how the different angular distribution of the three considered Galactic components reflects in the pattern of the straylight signal TOD, more or less “diffuse” according to the considered component.

Similar results are found for all the considered beam patterns, but with a peak-to-peak and RMS straylight signal significantly dependent on the adopted pattern shape. Instead of reporting the full simulation results, a concise comparison between the results obtained for the whole set of optical configurations is reported in the next section.

⁵ On the contrary, as obvious, the best possible knowledge of the antenna pattern, including all possible effects, from those due dust and molecular contamination on mirror surfaces to those related to the mirror roughness and temperature behaviour, should to be taken into account in the final data analysis.

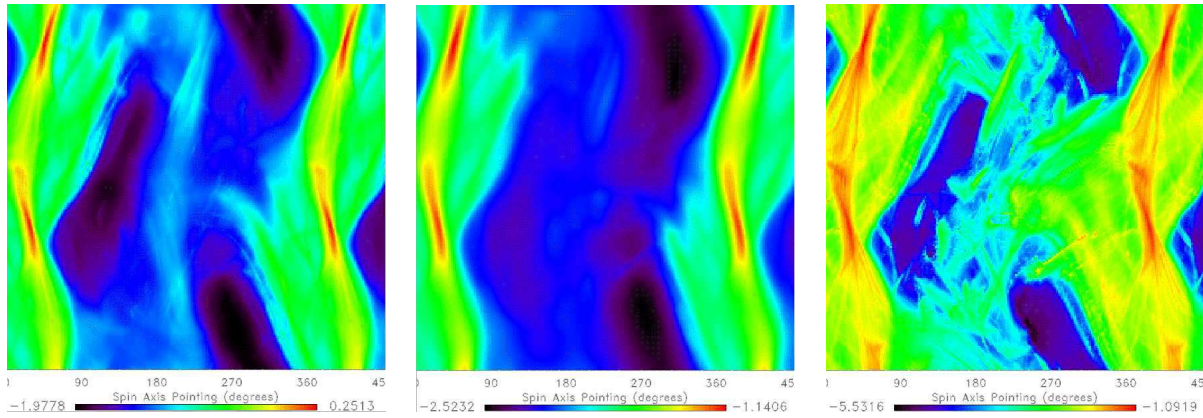


Fig. 4. Synthetic view of the data stream in terms of decimal logarithm of the antenna temperature in μK from all scan circles for the different Galactic components. The ecliptic coordinates properly refer here to the latitude of the telescope LOS (for graphic purposes, in this plot the range between -85° and -255° refer to the second half of each scan circle) and to the its longitude shift with respect to its initial direction, or equivalently to the shift of the spin axis pointing direction. We report here the straylight signal in the far sidelobes computed by including the first, second and third order optical interactions for the beam LFI9 9B (see also the text).

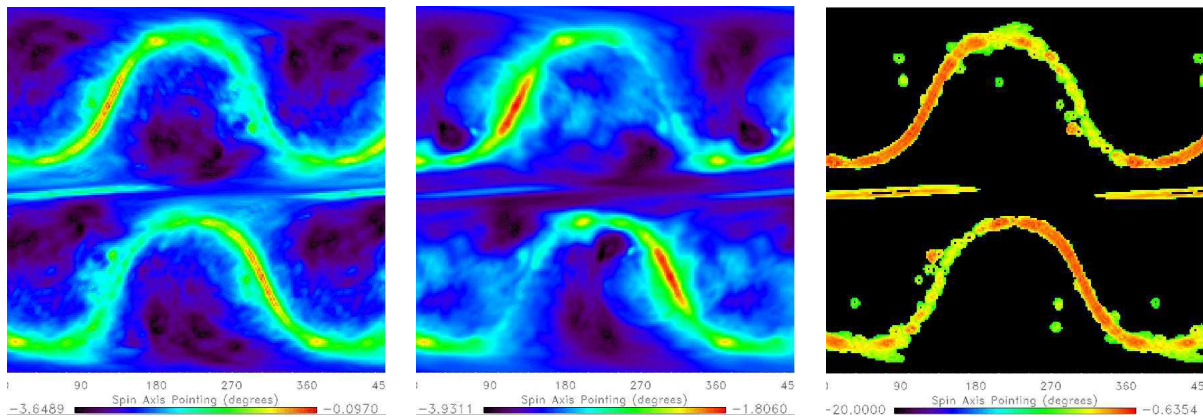


Fig. 5. The same as in Fig. 4, but for the signal from the intermediate pattern. In this case, Galactic HII regions produce a quite localized straylight contamination, null far from these sources and arbitrarily set to $10^{-20}\mu\text{K}$ for graphic purposes (as in Fig. 4, we report here the decimal logarithm of the antenna temperature in μK ; see also the text).

4. Comparison between different antenna patterns and foreground components

The statistical moments of the straylight signal TOD and its peak-to-peak value are reported in Tables 1–7 for our whole set of optical configurations at 100 GHz [in the tables, the data referring to the global straylight effect from intermediate pattern plus far sidelobes (I + F) are derived including also the contribution from the third order optical

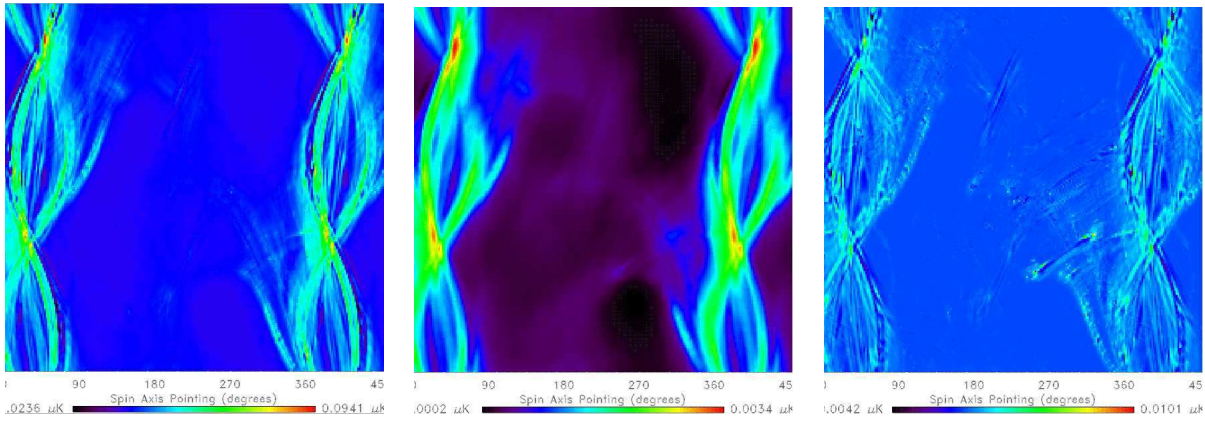


Fig. 6. The same as in Fig. 4, but referring to the difference between the straylight signals computed by including or not the third order optical interaction (the antenna temperature in μK in linear scale is here reported; see also the text).

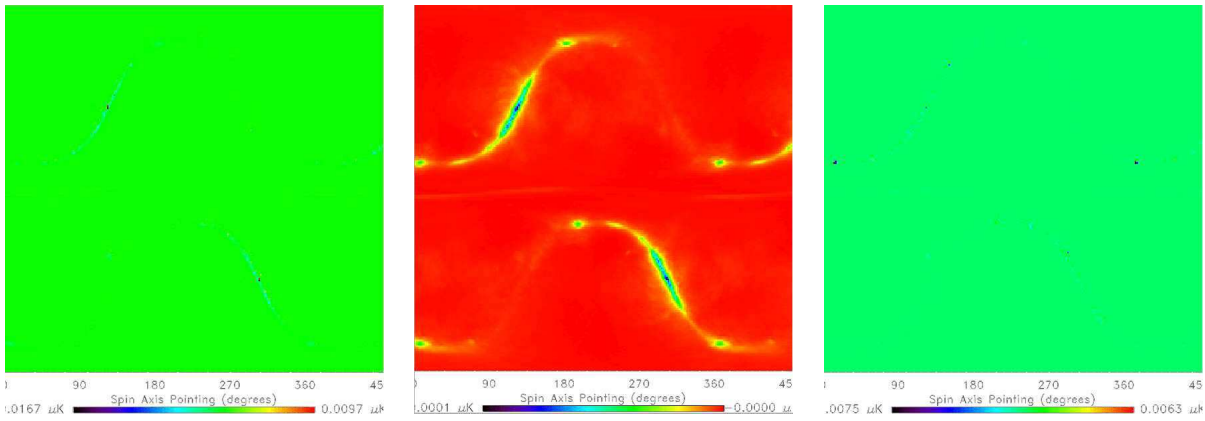


Fig. 7. The same as in Fig. 6, but for the signal from the intermediate pattern (see also the text).

interactions, when available]. Table 8 summarizes the basic information contained in the above tables as functions of the edge taper.

As evident from the tables, the contamination from the far sidelobes is much more relevant than that from the intermediate pattern when the RMS of the TOD is considered; by looking at the peak-to-peak of the straylight signal, the contamination from the far sidelobes is larger by a factor of few units or comparable to that from the intermediate pattern. The larger impact of the far sidelobes with respect to the intermediate pattern is particularly remarkable for the case of the diffuse Galactic components, while it is less evident in the case the map of free-free emission from Galactic HII regions. We find in fact a quite general behaviour: more diffuse the component and more relevant the straylight contamination from far sidelobes with respect to the intermediate pattern.

On the contrary, the skewness and kurtosis indices are larger for the straylight contamination from the intermediate pattern because they are more sensitive to localized

Please give a shorter version with: \authorrunning and/or \titilerunning prior to \maketitle

Table 1. Statistical moments and peak-to-peak of the simulated TOD (antenna temperature expressed in μK) from intermediate and far sidelobes of the simulated beam pattern LFI9 9A at 100 GHz for different Galactic components. The row labelled with “I123” (“I12”) refers to the signal in the intermediate beam computed taking into account the first, second and third (first and second) order optical interactions. The row labelled with “F123” (“F12”) refers to the signal in the far sidelobes computed taking into account the first, second and third (first and second) order optical interactions (see also the text).

LFI9 9A						
BEAM					SKEWNESS	KURTOSIS
REGION	AVERAGE	VARIANCE	RMS	PEAK-TO-PEAK	INDEX	INDEX
DUST + DIFFUSE FREE-FREE EMISSION						
I12	2.27×10^{-3}	5.81×10^{-5}	7.63×10^{-3}	2.61×10^{-1}	$9.45 \times 10^{+0}$	$1.33 \times 10^{+2}$
F123	6.71×10^{-2}	4.77×10^{-3}	6.90×10^{-2}	5.88×10^{-1}	$1.88 \times 10^{+0}$	$4.92 \times 10^{+0}$
F12	6.40×10^{-2}	4.49×10^{-3}	6.70×10^{-2}	5.68×10^{-1}	$1.89 \times 10^{+0}$	$4.90 \times 10^{+0}$
I + F	6.93×10^{-2}	4.83×10^{-3}	6.95×10^{-2}	5.88×10^{-1}	$1.81 \times 10^{+0}$	$4.59 \times 10^{+0}$
DIFFUSE SYNCHROTRON EMISSION						
I12	2.10×10^{-4}	1.05×10^{-7}	3.24×10^{-4}	4.66×10^{-3}	$6.59 \times 10^{+0}$	$5.64 \times 10^{+1}$
F123	5.87×10^{-3}	1.65×10^{-5}	4.07×10^{-3}	2.32×10^{-2}	$1.27 \times 10^{+0}$	$1.11 \times 10^{+0}$
F12	5.60×10^{-3}	1.55×10^{-5}	3.94×10^{-3}	2.24×10^{-2}	$1.29 \times 10^{+0}$	$1.13 \times 10^{+0}$
I + F	6.08×10^{-3}	1.67×10^{-5}	4.09×10^{-3}	2.31×10^{-2}	$1.22 \times 10^{+0}$	9.44×10^{-1}
HII REGIONS						
I12	7.70×10^{-5}	7.45×10^{-7}	8.63×10^{-4}	8.05×10^{-2}	$4.14 \times 10^{+1}$	$2.67 \times 10^{+3}$
F123	2.13×10^{-3}	7.14×10^{-6}	2.67×10^{-3}	2.67×10^{-2}	$1.93 \times 10^{+0}$	$5.87 \times 10^{+0}$
F12	2.02×10^{-3}	6.69×10^{-6}	2.59×10^{-3}	2.61×10^{-2}	$1.94 \times 10^{+0}$	$5.82 \times 10^{+0}$
I + F	2.20×10^{-3}	7.99×10^{-6}	2.83×10^{-3}	8.67×10^{-2}	$2.97 \times 10^{+0}$	$3.27 \times 10^{+1}$
SUM OF THE ABOVE COMPONENTS						
I12	2.55×10^{-3}	7.02×10^{-5}	8.38×10^{-3}	2.94×10^{-1}	$9.51 \times 10^{+0}$	$1.37 \times 10^{+2}$
F123	7.51×10^{-2}	5.71×10^{-3}	7.56×10^{-2}	6.38×10^{-1}	$1.84 \times 10^{+0}$	$4.66 \times 10^{+0}$
F12	7.16×10^{-2}	5.38×10^{-3}	7.33×10^{-2}	6.16×10^{-1}	$1.85 \times 10^{+0}$	$4.64 \times 10^{+0}$
I + F	7.76×10^{-2}	5.79×10^{-3}	7.61×10^{-2}	6.38×10^{-1}	$1.78 \times 10^{+0}$	$4.34 \times 10^{+0}$

features. As expected, these indices are larger for the free-free emission from Galactic HII regions than for the more diffuse components.

For a couple of representative cases, LFI9 9B and LFI4 4A, we evaluated the straylight signal on the basis of the WMAP map at 94 GHz for the intermediate pattern and far sidelobes, respectively (see Tables 2 and 4). For the signal in the intermediate pattern, we find a straylight contamination larger by a factor $\simeq 1.6$ in terms of RMS (but essentially unchanged in terms of peak-to-peak). It is interesting to note that in the case of the WMAP map, since the 94 GHz channel has a low level of Galactic foreground

Table 2. The same as in Table 1, but for the indicated simulated beam pattern. Note how the straylight in the intermediate pattern I123 the GSC is just smaller when the third order optical interaction is included (compare I123 with I12). This is due to a small decrease ($\simeq 0.4\%$) of the integrated antenna pattern response in that pattern region when the third order optical interaction is taken into account because of the combination in amplitude and phase of the various contributions, producing an overall antenna response – different from a simple sum of the powers of the various contributions – that typically increases with the number of considered contributions, as occurs here in the case of far sidelobes, but not necessarily does. For the straylight in the intermediate pattern we report also the result based on the WMAP map at 94 GHz, including all components.

LF19 9B						
BEAM					SKEWNESS	KURTOSIS
REGION	AVERAGE	VARIANCE	RMS	PEAK-TO-PEAK	INDEX	INDEX
DUST + DIFFUSE FREE-FREE EMISSION						
I123	7.54×10^{-3}	6.38×10^{-4}	2.53×10^{-2}	8.00×10^{-1}	$9.24 \times 10^{+0}$	$1.23 \times 10^{+2}$
I12	7.57×10^{-3}	6.41×10^{-4}	2.53×10^{-2}	7.90×10^{-1}	$9.18 \times 10^{+0}$	$1.21 \times 10^{+2}$
F123	1.45×10^{-1}	3.31×10^{-2}	1.82×10^{-1}	$1.77 \times 10^{+0}$	$2.88 \times 10^{+0}$	$1.19 \times 10^{+1}$
F12	1.35×10^{-1}	3.03×10^{-2}	1.74×10^{-1}	$1.73 \times 10^{+0}$	$2.96 \times 10^{+0}$	$1.26 \times 10^{+1}$
I + F	1.53×10^{-1}	3.35×10^{-2}	1.83×10^{-1}	$1.77 \times 10^{+0}$	$2.77 \times 10^{+0}$	$1.12 \times 10^{+1}$
DIFFUSE SYNCHROTRON EMISSION						
I123	6.96×10^{-4}	1.16×10^{-6}	1.08×10^{-3}	1.55×10^{-2}	$6.58 \times 10^{+0}$	$5.63 \times 10^{+1}$
I12	6.99×10^{-4}	1.17×10^{-6}	1.08×10^{-3}	1.55×10^{-2}	$6.57 \times 10^{+0}$	$5.61 \times 10^{+1}$
F123	1.27×10^{-2}	1.06×10^{-4}	1.03×10^{-2}	6.93×10^{-2}	$1.89 \times 10^{+0}$	$3.97 \times 10^{+0}$
F12	1.18×10^{-2}	9.63×10^{-5}	9.81×10^{-3}	6.71×10^{-2}	$1.95 \times 10^{+0}$	$4.24 \times 10^{+0}$
I + F	1.34×10^{-2}	1.07×10^{-4}	1.03×10^{-2}	6.91×10^{-2}	$1.81 \times 10^{+0}$	$3.67 \times 10^{+0}$
HII REGIONS						
I123	2.58×10^{-4}	7.31×10^{-6}	2.70×10^{-3}	2.32×10^{-1}	$3.57 \times 10^{+1}$	$2.03 \times 10^{+3}$
I12	2.59×10^{-4}	7.31×10^{-6}	2.70×10^{-3}	2.32×10^{-1}	$3.55 \times 10^{+1}$	$2.02 \times 10^{+3}$
F123	4.45×10^{-3}	4.70×10^{-5}	6.86×10^{-3}	8.09×10^{-2}	$3.18 \times 10^{+0}$	$1.60 \times 10^{+1}$
F12	4.13×10^{-3}	4.27×10^{-5}	6.54×10^{-3}	7.64×10^{-2}	$3.27 \times 10^{+0}$	$1.68 \times 10^{+1}$
I + F	4.71×10^{-3}	5.45×10^{-5}	7.38×10^{-3}	2.45×10^{-1}	$4.38 \times 10^{+0}$	$5.24 \times 10^{+1}$
SUM OF THE ABOVE COMPONENTS						
I123	8.49×10^{-3}	7.70×10^{-4}	2.77×10^{-2}	8.94×10^{-1}	$9.24 \times 10^{+0}$	$1.25 \times 10^{+2}$
I12	8.53×10^{-3}	7.72×10^{-4}	2.78×10^{-2}	8.84×10^{-1}	$9.18 \times 10^{+0}$	$1.22 \times 10^{+2}$
F123	1.62×10^{-1}	3.94×10^{-2}	1.99×10^{-1}	$1.92 \times 10^{+0}$	$2.83 \times 10^{+0}$	$1.14 \times 10^{+1}$
F12	1.51×10^{-1}	3.61×10^{-2}	1.90×10^{-1}	$1.87 \times 10^{+0}$	$2.90 \times 10^{+0}$	$1.21 \times 10^{+1}$
I + F	1.71×10^{-1}	3.99×10^{-2}	2.00×10^{-1}	$1.92 \times 10^{+0}$	$2.72 \times 10^{+0}$	$1.08 \times 10^{+1}$
WMAP AT 94GHz						
I123	1.92×10^{-2}	1.97×10^{-3}	4.44×10^{-2}	8.65×10^{-1}	$5.31 \times 10^{+0}$	$3.97 \times 10^{+1}$

Table 3. The same as in Table 1, but for the indicated simulated beam pattern.

LFI9 9C						
BEAM					SKEWNESS	KURTOSIS
REGION	AVERAGE	VARIANCE	RMS	PEAK-TO-PEAK	INDEX	INDEX
DUST + DIFFUSE FREE-FREE EMISSION						
I12	2.20×10^{-2}	5.42×10^{-3}	7.36×10^{-2}	$2.02 \times 10^{+0}$	$8.87 \times 10^{+0}$	$1.06 \times 10^{+2}$
F123	4.71×10^{-1}	4.17×10^{-1}	6.46×10^{-1}	$5.84 \times 10^{+0}$	$3.00 \times 10^{+0}$	$1.24 \times 10^{+1}$
F12	4.34×10^{-1}	3.80×10^{-1}	6.16×10^{-1}	$5.70 \times 10^{+0}$	$3.10 \times 10^{+0}$	$1.32 \times 10^{+1}$
I + F	4.93×10^{-1}	4.20×10^{-1}	6.48×10^{-1}	$5.84 \times 10^{+0}$	$2.92 \times 10^{+0}$	$1.19 \times 10^{+1}$
DIFFUSE SYNCHROTRON EMISSION						
I12	2.04×10^{-3}	9.95×10^{-6}	3.15×10^{-3}	4.59×10^{-2}	$6.65 \times 10^{+0}$	$5.76 \times 10^{+1}$
F123	4.12×10^{-2}	1.33×10^{-3}	3.65×10^{-2}	2.45×10^{-1}	$2.04 \times 10^{+0}$	$4.61 \times 10^{+0}$
F12	3.79×10^{-2}	1.19×10^{-3}	3.45×10^{-2}	2.38×10^{-1}	$2.12 \times 10^{+0}$	$5.03 \times 10^{+0}$
I + F	4.32×10^{-2}	1.33×10^{-3}	3.65×10^{-2}	2.44×10^{-1}	$1.98 \times 10^{+0}$	$4.39 \times 10^{+0}$
HII REGIONS						
I12	7.54×10^{-4}	5.36×10^{-5}	7.32×10^{-3}	5.46×10^{-1}	$2.98 \times 10^{+1}$	$1.41 \times 10^{+3}$
F123	1.43×10^{-2}	5.92×10^{-4}	2.43×10^{-2}	2.75×10^{-1}	$3.29 \times 10^{+0}$	$1.58 \times 10^{+1}$
F12	1.31×10^{-2}	5.37×10^{-4}	2.32×10^{-2}	2.59×10^{-1}	$3.39 \times 10^{+0}$	$1.68 \times 10^{+1}$
I + F	1.50×10^{-2}	6.47×10^{-4}	2.54×10^{-2}	5.91×10^{-1}	$3.62 \times 10^{+0}$	$2.42 \times 10^{+1}$
SUM OF THE ABOVE COMPONENTS						
I12	2.48×10^{-2}	6.52×10^{-3}	8.08×10^{-2}	$2.26 \times 10^{+0}$	$8.85 \times 10^{+0}$	$1.07 \times 10^{+2}$
F123	5.26×10^{-1}	4.97×10^{-1}	7.05×10^{-1}	$6.35 \times 10^{+0}$	$2.96 \times 10^{+0}$	$1.20 \times 10^{+1}$
F12	4.85×10^{-1}	4.52×10^{-1}	6.72×10^{-1}	$6.18 \times 10^{+0}$	$3.05 \times 10^{+0}$	$1.27 \times 10^{+1}$
I + F	5.51×10^{-1}	5.00×10^{-1}	7.07×10^{-1}	$6.35 \times 10^{+0}$	$2.88 \times 10^{+0}$	$1.15 \times 10^{+1}$

contamination, the contribution to straylight from CMB fluctuations clearly appears (see Fig. 8) far from the Galactic plane, where the straylight signal is negligible in the case of the simulation carried out by using the three Galactic templates (on the contrary, this effect is not evident at 30 GHz, see Fig. B.1 in Appendix B). If we set to zero the values of the TOD samples with signal smaller than $\simeq 0.15\mu\text{K}$ (the maximum value of straylight far from the Galactic plane in the right panel of Fig. 8) we obtain a RMS straylight of $\simeq 0.024\mu\text{K}$, quite close to the RMS straylight value of $\simeq 0.028\mu\text{K}$ obtained in the case of the sum of the three adopted Galactic templates (see Table 2). This means that main contribution to the factor $\simeq 1.6$ of discrepancy in the RMS of the straylight signal found by adopting the three Galactic templates or the WMAP map at 94 GHz is mainly produced by the CMB anisotropy.

In the case of the straylight in the far sidelobes we find a straylight contamination larger only by a factor ~ 1.3 in the case of the WMAP map than in the case of the sum of the three adopted Galactic templates, in terms of both RMS and peak-to-peak. The above CMB anisotropy effect is not evident. On the contrary, the regions at low straylight signal

Table 4. The same as in Table 1, but for the indicated simulated beam pattern. For the straylight in the far sidelobes we report also the result based on the WMAP map at 94 GHz, including all components.

LFI4 4A						
BEAM					SKEWNESS	KURTOSIS
REGION	AVERAGE	VARIANCE	RMS	PEAK-TO-PEAK	INDEX	INDEX
DUST + DIFFUSE FREE-FREE EMISSION						
I12	5.03×10^{-4}	2.88×10^{-6}	1.70×10^{-3}	5.71×10^{-2}	$9.19 \times 10^{+0}$	$1.22 \times 10^{+2}$
F123	1.42×10^{-2}	1.83×10^{-4}	1.35×10^{-2}	1.02×10^{-1}	$1.73 \times 10^{+0}$	$4.00 \times 10^{+0}$
F12	1.24×10^{-2}	1.54×10^{-4}	1.24×10^{-2}	1.02×10^{-1}	$2.02 \times 10^{+0}$	$5.84 \times 10^{+0}$
I + F	1.47×10^{-2}	1.87×10^{-4}	1.37×10^{-2}	1.02×10^{-1}	$1.65 \times 10^{+0}$	$3.58 \times 10^{+0}$
DIFFUSE SYNCHROTRON EMISSION						
I12	4.62×10^{-5}	5.13×10^{-9}	7.16×10^{-5}	1.07×10^{-3}	$6.72 \times 10^{+0}$	$5.96 \times 10^{+1}$
F123	1.24×10^{-3}	5.89×10^{-7}	7.76×10^{-4}	4.57×10^{-3}	$1.08 \times 10^{+0}$	7.86×10^{-1}
F12	1.09×10^{-3}	4.86×10^{-7}	6.97×10^{-4}	4.38×10^{-3}	$1.23 \times 10^{+0}$	$1.44 \times 10^{+0}$
I + F	1.29×10^{-3}	6.02×10^{-7}	7.76×10^{-4}	4.56×10^{-3}	$1.02 \times 10^{+0}$	5.69×10^{-1}
HII REGIONS						
I12	1.77×10^{-5}	2.99×10^{-8}	1.73×10^{-4}	1.24×10^{-2}	$3.11 \times 10^{+1}$	$1.51 \times 10^{+3}$
F123	4.85×10^{-4}	3.69×10^{-7}	6.07×10^{-4}	8.04×10^{-3}	$1.83 \times 10^{+0}$	$4.34 \times 10^{+0}$
F12	4.19×10^{-4}	2.97×10^{-7}	5.45×10^{-4}	7.74×10^{-3}	$2.09 \times 10^{+0}$	$6.13 \times 10^{+0}$
I + F	5.03×10^{-4}	4.04×10^{-7}	6.36×10^{-4}	1.41×10^{-2}	$2.32 \times 10^{+0}$	$1.42 \times 10^{+1}$
SUM OF THE ABOVE COMPONENTS						
I12	5.67×10^{-4}	3.47×10^{-6}	1.86×10^{-3}	6.51×10^{-2}	$9.18 \times 10^{+0}$	$1.24 \times 10^{+2}$
F123	1.59×10^{-2}	2.20×10^{-4}	1.48×10^{-2}	1.10×10^{-1}	$1.70 \times 10^{+0}$	$3.77 \times 10^{+0}$
F12	1.39×10^{-2}	1.85×10^{-4}	1.36×10^{-2}	1.11×10^{-1}	$1.97 \times 10^{+0}$	$5.52 \times 10^{+0}$
I + F	1.65×10^{-2}	2.25×10^{-4}	1.50×10^{-2}	1.10×10^{-1}	$1.61 \times 10^{+0}$	$3.36 \times 10^{+0}$
WMAP AT 94 GHz						
F123	2.75×10^{-2}	3.37×10^{-4}	1.83×10^{-2}	1.51×10^{-1}	$1.33 \times 10^{+0}$	$3.00 \times 10^{+0}$

in the case of the simulation based on the WMAP map show a pattern that, although with different signal values, is quite similar to that found in the same regions by using the Galactic templates. This indicates that the main difference found in this case is due to the adopted model of Galactic templates, in agreement with the idea that CMB anisotropies (and also extragalactic bright sources and fluctuations, minimum at about 100–200 GHz) contained in the WMAP map, can produce only minor contaminations, compared to the Galactic signal, because of their smaller power at large angular scales which implies that positive and negative fluctuations partially compensate inside the relatively large antenna pattern solid angles relevant for this kind of straylight contamination.

By exploiting our set of optical configurations and taking into account the correction factor found on the basis of the WMAP map, we find a linear approximation describing

Please give a shorter version with: \authorrunning and/or \titilerunning prior to \maketitle

Table 5. The same as in Table 1, but for the indicated simulated beam pattern.

LFI4 4B						
BEAM					SKEWNESS	KURTOSIS
REGION	AVERAGE	VARIANCE	RMS	PEAK-TO-PEAK	INDEX	INDEX
DUST + DIFFUSE FREE-FREE EMISSION						
I12	1.28×10^{-2}	1.97×10^{-3}	4.44×10^{-2}	$1.46 \times 10^{+0}$	$9.80 \times 10^{+0}$	$1.42 \times 10^{+2}$
F12	1.68×10^{-1}	3.64×10^{-2}	1.91×10^{-1}	$1.51 \times 10^{+0}$	$2.39 \times 10^{+0}$	$7.90 \times 10^{+0}$
I + F	1.81×10^{-1}	3.86×10^{-2}	1.96×10^{-1}	$1.58 \times 10^{+0}$	$2.21 \times 10^{+0}$	$6.71 \times 10^{+0}$
DIFFUSE SYNCHROTRON EMISSION						
I12	1.17×10^{-3}	3.33×10^{-6}	1.82×10^{-3}	2.80×10^{-2}	$6.80 \times 10^{+0}$	$6.11 \times 10^{+1}$
F12	1.47×10^{-2}	1.14×10^{-4}	1.07×10^{-2}	6.64×10^{-2}	$1.50 \times 10^{+0}$	$2.39 \times 10^{+0}$
I + F	1.59×10^{-2}	1.18×10^{-4}	1.09×10^{-2}	6.60×10^{-2}	$1.38 \times 10^{+0}$	$1.86 \times 10^{+0}$
HII REGIONS						
I12	4.53×10^{-4}	2.17×10^{-5}	4.65×10^{-3}	3.89×10^{-1}	$3.24 \times 10^{+1}$	$1.73 \times 10^{+3}$
F12	5.48×10^{-3}	6.43×10^{-5}	8.02×10^{-3}	6.53×10^{-2}	$2.50 \times 10^{+0}$	$8.11 \times 10^{+0}$
I + F	5.93×10^{-3}	8.78×10^{-5}	9.37×10^{-3}	4.11×10^{-1}	$5.89 \times 10^{+0}$	$1.25 \times 10^{+2}$
SUM OF THE ABOVE COMPONENTS						
I12	1.44×10^{-2}	2.38×10^{-3}	4.88×10^{-2}	$1.65 \times 10^{+0}$	$9.81 \times 10^{+0}$	$1.45 \times 10^{+2}$
F12	1.89×10^{-1}	4.35×10^{-2}	2.09×10^{-1}	$1.63 \times 10^{+0}$	$2.34 \times 10^{+0}$	$7.53 \times 10^{+0}$
I + F	2.03×10^{-1}	4.63×10^{-2}	2.15×10^{-1}	$1.79 \times 10^{+0}$	$2.17 \times 10^{+0}$	$6.41 \times 10^{+0}$

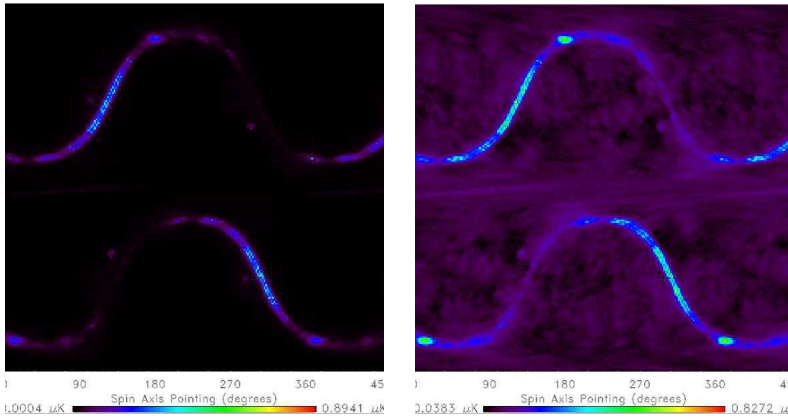


Fig. 8. The same as in Fig. 5 but for the sum of the three Galactic templates and for the WMAP map at 94 GHz where the contribution from CMB anisotropy appears (the antenna temperature in μK in linear scale is here reported; see also the text).

quite well the dependence of the RMS and the peak-to-peak values of the GSC at 100 GHz on the (per cent) fractional contribution, $f_{\%}$, to the integrated antenna pattern response from the considered pattern region (see also Fig. 9):

$$\text{peak-to-peak} \simeq 5.3\mu\text{K} \times f_{\%} \simeq 175\mu\text{K} \times \text{LET} \quad (3)$$

$$\text{rms} \simeq 0.62\mu\text{K} \times f_{\%} \simeq 21\mu\text{K} \times \text{LET}, \quad (4)$$

Table 6. The same as in Table 1, but for the indicated simulated beam pattern.

LFI4 4C						
BEAM					SKEWNESS	KURTOSIS
REGION	AVERAGE	VARIANCE	RMS	PEAK-TO-PEAK	INDEX	INDEX
DUST + DIFFUSE FREE-FREE EMISSION						
I12	9.56×10^{-3}	1.12×10^{-3}	3.34×10^{-2}	$1.13 \times 10^{+0}$	$9.96 \times 10^{+0}$	$1.49 \times 10^{+2}$
F12	1.08×10^{-1}	1.64×10^{-2}	1.28×10^{-1}	$1.03 \times 10^{+0}$	$2.55 \times 10^{+0}$	$8.77 \times 10^{+0}$
I + F	1.17×10^{-1}	1.76×10^{-2}	1.33×10^{-1}	$1.20 \times 10^{+0}$	$2.36 \times 10^{+0}$	$7.43 \times 10^{+0}$
DIFFUSE SYNCHROTRON EMISSION						
I12	8.75×10^{-4}	1.87×10^{-6}	1.37×10^{-3}	2.11×10^{-2}	$6.81 \times 10^{+0}$	$6.14 \times 10^{+1}$
F12	9.43×10^{-3}	5.01×10^{-5}	7.08×10^{-3}	4.49×10^{-2}	$1.64 \times 10^{+0}$	$2.90 \times 10^{+0}$
I + F	1.03×10^{-2}	5.21×10^{-5}	7.22×10^{-3}	4.46×10^{-2}	$1.49 \times 10^{+0}$	$2.27 \times 10^{+0}$
HII REGIONS						
I12	3.40×10^{-4}	1.24×10^{-5}	3.53×10^{-3}	2.93×10^{-1}	$3.24 \times 10^{+1}$	$1.71 \times 10^{+3}$
F12	3.51×10^{-3}	2.93×10^{-5}	5.41×10^{-3}	4.55×10^{-2}	$2.69 \times 10^{+0}$	$9.26 \times 10^{+0}$
I + F	3.85×10^{-3}	4.25×10^{-5}	6.52×10^{-3}	3.08×10^{-1}	$7.07 \times 10^{+0}$	$1.71 \times 10^{+2}$
SUM OF THE ABOVE COMPONENTS						
I12	1.08×10^{-2}	1.35×10^{-3}	3.67×10^{-2}	$1.27 \times 10^{+0}$	$9.98 \times 10^{+0}$	$1.52 \times 10^{+2}$
F12	1.21×10^{-1}	1.96×10^{-2}	1.40×10^{-1}	$1.12 \times 10^{+0}$	$2.50 \times 10^{+0}$	$8.38 \times 10^{+0}$
I + F	1.32×10^{-1}	2.11×10^{-2}	1.45×10^{-1}	$1.35 \times 10^{+0}$	$2.32 \times 10^{+0}$	$7.13 \times 10^{+0}$

for the far sidelobes, and

$$\text{peak-to-peak} \simeq 28\mu\text{K} \times f_{\%} \simeq 98\mu\text{K} \times \text{LET} \quad (5)$$

$$rms \simeq 0.86\mu\text{K} \times f_{\%} \simeq 3\mu\text{K} \times \text{LET}, \quad (6)$$

for the intermediate pattern ⁶, where eqs. (1)–(5) of Paper I are taken into account in the last equalities of these equations (the LET is here referred to a taper at an angle of 24° from the feed axis). The numerical coefficients in eq. (6) can be multiplied by $\simeq 1.6$ to include also the straylight contribution in the intermediate pattern from CMB fluctuations.

Clearly, in the cosmological window the GSC contamination is less than that in the lowest and highest PLANCK frequency channels and so its impact on CMB power spectrum recovery (see Burigana et al. 2001 for an analysis of GSC impact on the power spectrum recovery and Fourier decomposition of scan circle data at the lowest PLANCK frequency channel). On the other hand, the ultimate goal of PLANCK, and in general of future CMB anisotropy experiments after WMAP, is not only the power spectrum recovery but also a detailed imaging of the last scattering surface and a detailed study of the

⁶ In these fits we adopt, for uniformity, the numbers found by considering the first and second order optical interactions, available for the all cases.

Table 7. The same as in Table 1, but for the indicated simulated beam pattern.

LFI4 4D						
BEAM					SKEWNESS	KURTOSIS
REGION	AVERAGE	VARIANCE	RMS	PEAK-TO-PEAK	INDEX	INDEX
DUST + DIFFUSE FREE-FREE EMISSION						
I12	1.19×10^{-2}	1.73×10^{-3}	4.16×10^{-2}	$1.41 \times 10^{+0}$	$9.93 \times 10^{+0}$	$1.48 \times 10^{+2}$
F12	1.47×10^{-1}	3.10×10^{-2}	1.76×10^{-1}	$1.43 \times 10^{+0}$	$2.60 \times 10^{+0}$	$9.10 \times 10^{+0}$
I + F	1.59×10^{-1}	3.28×10^{-2}	1.81×10^{-1}	$1.50 \times 10^{+0}$	$2.41 \times 10^{+0}$	$7.82 \times 10^{+0}$
DIFFUSE SYNCHROTRON EMISSION						
I12	1.09×10^{-3}	2.91×10^{-6}	1.71×10^{-3}	2.62×10^{-2}	$6.81 \times 10^{+0}$	$6.13 \times 10^{+1}$
F12	1.28×10^{-2}	9.39×10^{-5}	9.69×10^{-3}	6.22×10^{-2}	$1.66 \times 10^{+0}$	$3.04 \times 10^{+0}$
I + F	1.39×10^{-2}	9.70×10^{-5}	9.85×10^{-3}	6.17×10^{-2}	$1.53 \times 10^{+0}$	$2.46 \times 10^{+0}$
HII REGIONS						
I12	4.24×10^{-4}	1.94×10^{-5}	4.40×10^{-3}	3.67×10^{-1}	$3.27 \times 10^{+1}$	$1.75 \times 10^{+3}$
F12	4.80×10^{-3}	5.55×10^{-5}	7.45×10^{-3}	6.36×10^{-2}	$2.73 \times 10^{+0}$	$9.59 \times 10^{+0}$
I + F	5.22×10^{-3}	7.61×10^{-5}	8.73×10^{-3}	3.88×10^{-1}	$6.26 \times 10^{+0}$	$1.35 \times 10^{+2}$
SUM OF THE ABOVE COMPONENTS						
I12	1.34×10^{-2}	2.09×10^{-3}	4.57×10^{-2}	$1.58 \times 10^{+0}$	$9.96 \times 10^{+0}$	$1.52 \times 10^{+2}$
F12	1.65×10^{-1}	3.70×10^{-2}	1.92×10^{-1}	$1.56 \times 10^{+0}$	$2.55 \times 10^{+0}$	$8.70 \times 10^{+0}$
I + F	1.78×10^{-1}	3.92×10^{-2}	1.98×10^{-1}	$1.69 \times 10^{+0}$	$2.37 \times 10^{+0}$	$7.49 \times 10^{+0}$

Table 8. RMS and peak-to-peak of the simulated TOD (antenna temperature expressed in μK) from intermediate, far sidelobes and both of them of the all simulated beam patterns at 100 GHz for sum of the three considered templates of Galactic components as functions of the edge taper. We neglect here the contribution from the third order optical interactions since only first and second order optical interactions have been evaluated for the all optical designs.

SUMMARY TABLE							
BEAM	ET	I	I	F	F	I + F	I + F
	dB @ 24°	RMS	PEAK-TO-PEAK	RMS	PEAK-TO-PEAK	RMS	PEAK-TO-PEAK
LFI9 9A	25.5	8.38×10^{-3}	2.94×10^{-1}	7.33×10^{-2}	6.16×10^{-1}	7.61×10^{-2}	6.38×10^{-1}
LFI9 9B	19.0	2.78×10^{-2}	8.84×10^{-1}	1.90×10^{-1}	$1.87 \times 10^{+0}$	2.00×10^{-1}	$1.92 \times 10^{+0}$
LFI9 9C	15.0	8.08×10^{-2}	$2.26 \times 10^{+0}$	6.72×10^{-1}	$6.18 \times 10^{+0}$	7.07×10^{-1}	$6.35 \times 10^{+0}$
LFI4 4A	28.3	1.86×10^{-3}	6.51×10^{-2}	1.36×10^{-2}	1.11×10^{-1}	1.50×10^{-2}	1.10×10^{-1}
LFI4 4B	19.0	4.88×10^{-2}	$1.65 \times 10^{+0}$	2.09×10^{-1}	$1.63 \times 10^{+0}$	2.15×10^{-1}	$1.79 \times 10^{+0}$
LFI4 4C	19.0	3.67×10^{-2}	$1.27 \times 10^{+0}$	1.40×10^{-1}	$1.12 \times 10^{+0}$	1.45×10^{-1}	$1.35 \times 10^{+0}$
LFI4 4D	19.0	4.57×10^{-2}	$1.58 \times 10^{+0}$	1.92×10^{-1}	$1.56 \times 10^{+0}$	1.98×10^{-1}	$1.69 \times 10^{+0}$

whole statistical information, cosmological and astrophysical, contained in the frequency maps. For this reason, the PLANCK requirement on the maximum acceptable level of

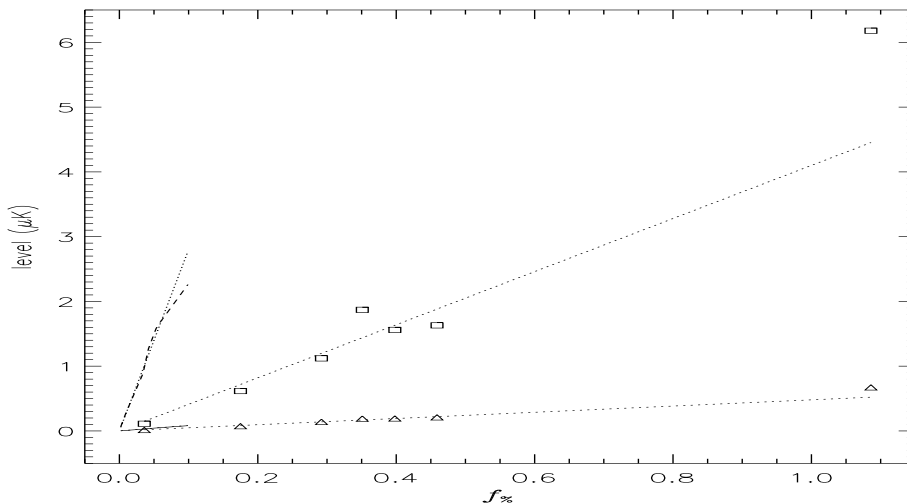


Fig. 9. Dependence of the RMS (solid line for the intermediate pattern and triangles for the far sidelobes) and the peak-to-peak values (dashed line for the intermediate pattern and squares for the far sidelobes) of the GSC at 100 GHz on the (per cent) fractional contribution to the integrated antenna pattern response from the considered pattern region and corresponding linear approximations (dotted lines).

systematic effect contamination is of few μK , in order to avoid spurious signals at a level comparable with the PLANCK sensitivity.

Among the set of analyzed optical configurations we can identify a subsample which reaches a good trade-off between the angular resolution (see Table 2 of Paper I) and the suppression of the straylight contamination.

In the case of LFI9 the configuration 9B shows a global peak-to-peak (RMS) GSC less than about $2\mu\text{K}$ ($0.2\mu\text{K}$) simultaneously reaching an angular resolution (FWHM) of $10.02'$. The configuration 9A shows a lower GSC, but with a worse angular resolution ($10.56'$), while the configuration 9C allows to reach a resolution of $9.54'$ but introducing a relatively large GSC, being its peak-to-peak (RMS) signal of about $7\mu\text{K}$ ($0.7\mu\text{K}$). The worse resolution for LFI4 with respect to LFI9 is due to the different location of the corresponding feed in the focal surface (see Mandolesi et al. 2000b). On the other hand, our analysis identifies a well defined optimal optical configuration (4C) that allows to reach the best angular resolution ($12.08'$) with the minimum GSC, i.e. a peak-to-peak (RMS) signal less than about $1.5\mu\text{K}$ ($0.15\mu\text{K}$).

In Appendix B we report also the results obtained for a simulation at 30 GHz. We find some qualitative differences between the GSC at these two frequencies, related to their optical behaviours and to the different role of the Galactic foregrounds.

An accurate computation of the GSC on PLANCK polarization data could be in principle carried out by using the formalism described in Challinor et al. (2000). On the other hand, since no microwave polarization surveys are currently available, a detailed

Please give a shorter version with: \authorrunning and/or \titilerunning prior to \maketitle

computation based on current simulated templates (see e.g. Giardino et al. 2002) may provide only indicative results. A first order analysis aimed to obtain a robust upper limit on the RMS GSC in the PLANCK LFI polarization data can be obtained with a simple argument. The signals, I_{ij} ($i = 1, 2$), in the four radiometers associated to a couple of LFI feeds symmetrically located on the focal plane can be expressed as:

$$\begin{aligned} 2I_{11} &= T + \delta T_{11}^s + (Q + \delta Q_{11}^s)\cos(2\phi_{11}) + (U + \delta U_{11}^s)\sin(2\phi_{11}) \\ 2I_{12} &= T + \delta T_{12}^s - (Q + \delta Q_{12}^s)\cos(2\phi_{11}) - (U + \delta U_{12}^s)\sin(2\phi_{11}) \\ 2I_{21} &= T + \delta T_{21}^s + (Q + \delta Q_{21}^s)\cos(2\phi_{21}) + (U + \delta U_{21}^s)\sin(2\phi_{21}) \\ 2I_{22} &= T + \delta T_{22}^s - (Q + \delta Q_{22}^s)\cos(2\phi_{21}) - (U + \delta U_{22}^s)\sin(2\phi_{21}). \end{aligned}$$

Here $\phi_{21} = \phi_{11} + \pi/4$, ϕ_{11} is the angle between the axis x_{bf} of the *beam frame* corresponding to the first feed and the direction of the parallel in the considered pointing direction, T , Q and U are the unpolarized signal and the Stokes parameters in the main beam, and the terms $\delta T_{ij}^s, \delta Q_{ij}^s, \delta U_{ij}^s$ account for the spurious contributions due to the Galactic straylight. For each pointing direction, they are different for the four radiometers because of the different level and orientation of the corresponding antenna patterns. The measure of the Stokes parameters Q and U is obtained by combining the signals in the four radiometers: $Q = (I_{11} - I_{12})\cos(2\phi_{11}) - (I_{21} - I_{22})\sin(2\phi_{11})$, $U = (I_{21} - I_{22})\cos(2\phi_{11}) + (I_{11} - I_{12})\sin(2\phi_{11})$. The Galactic synchrotron emission is partially polarized ($\sim 30\%$), while the Galactic free-free and thermal dust emission, most relevant at $\nu \gtrsim 50$ GHz, are only weakly polarized (a few %). Therefore, at least in the cosmological window, a Galactic straylight contamination relevant for the polarization measure mainly derives from the differences between the temperature straylight signals, δT_{ij}^s , in each pairs of radiometers associated to the same feed. Assuming a typical value $\sim 1/2$ for $\cos(2\phi_{11})$ and $\sin(2\phi_{11})$, we find a RMS GSC on Q and U similar to that found above for T [see eqs. (4) and (6)], to be considered as a pessimistic upper limit, corresponding to a difference of a factor $\simeq 2$ in the temperature straylight signals in each pair of radiometers.

We then conclude that, at least in terms of RMS and in the cosmological window, keeping at very low level the GSC in the temperature data directly assures an adequate suppression of the GSC in the polarization data.

5. Conclusions

Satellite CMB anisotropy missions, such as WMAP and PLANCK, and also the new generation of balloon-borne and ground experiments, make use of complex multi-frequency instruments at the focal surface of a meter class telescope to allow the joint study of CMB and foreground anisotropies, necessary for a high quality component separation. In the so-called ‘‘cosmological window’’, between ~ 70 GHz and ~ 300 GHz, where foreground

contamination is minimum, it is extremely important to reach the best angular resolution (necessary to measure the high order acoustic peaks of CMB anisotropy) achievable keeping at the same time the straylight contamination at acceptable levels (peak-to-peak of few μK).

By focusing, as a working case, on the 100 GHz channels of PLANCK LFI, we have presented here extensive simulations of the straylight contamination starting from a wide set of simulated optical configurations, described in Paper I, in order to find the best compromise between resolution and GSC.

By adopting some templates of Galactic foreground extrapolated from radio and IR surveys we found that it is possible to improve the angular resolution of about 5 – 7 % and to reach for example $10' - 12'$ of FWHM at 100 GHz by keeping the overall straylight contamination below the level of few μK in terms of peak-to-peak and about 10 times smaller in terms of RMS, as necessary to avoid systematic errors comparable with the PLANCK sensitivity.

We compared the level of straylight introduced by the different Galactic components for different beam regions and provided simple approximate relations giving the RMS and peak-to-peak levels of the GSC for the intermediate pattern and the far sidelobes as functions of the corresponding contributions to the integrated antenna pattern response, related to the edge taper.

For the considered optical designs, the most important straylight contamination derives from the far sidelobes, where the Galactic signal overwhelms the other straylight contributions (nevertheless, in the intermediate pattern, the straylight contamination from CMB fluctuations is found to be not negligible compared to the GSC).

We demonstrated that including the third order optical interactions changes only of few % the results of straylight analyses. As discussed in Paper I, this is extremely important for optical design optimization studies, proving that accurate enough optical simulations can be carried out by saving about 75% of the computational time without a relevant loss of accuracy.

Keeping at very low level the GSC in the temperature data directly assures a reliable suppression of the GSC in the polarization data, at least in terms of RMS. The CMB polarization angular power spectrum (ET , E , and B modes) recovery will be then not significantly affected by straylight.

The results at 100 GHz have been compared with those at 30 GHz, where the GSC is more critical, showing a peak-to-peak value at a level of $\simeq 5 - 7\mu\text{K}$. In comparison with previous analyses (see e.g. Burigana et al. 2001), this represents a relevant improvement in straylight rejection related to the optimization of the overall PLANCK optical scheme (Dubruel et al. 2000). Clearly, assuming different Galactic templates implies differences in the computed straylight signals. On the other hand, even for the quite different input maps adopted in these tests, differences larger than $\simeq 1 - 2\mu\text{K}$ are limited to quite

localized regions, close to the Galactic plane, where the CMB anisotropy is dominated by the very high Galactic signal in the main beam. This suggests that, even far from the “cosmological window”, a subtraction of the GSC well down to $\sim 1\mu\text{K}$ level could be obtained by evaluating with few iterations the straylight contamination signal for the maps directly derived from PLANCK observations, provided that the antenna pattern response could be quite accurately modelled.

Acknowledgements. Some of the results in this paper have been derived using the HEALPix (Gòrski et al. 1999).

Appendix A: Transformation rules between *telescope frame* and *beam frame*

Let \mathbf{s} be the unit vector, choosen outward the Sun direction, of the spin axis direction and \hat{k} that of the direction, z , of the telescope line of sight (LOS), pointing at an angle $\alpha \sim 85^\circ$ from the direction of \mathbf{s} .

On the plane tangent to the celestial sphere in the direction of the LOS we choose two coordinates x and y , respectively defined by the unit vector \hat{i} and \hat{j} according to the convention that the unit vector \hat{i} points always toward \mathbf{s} and that x, y, z is a standard Cartesian frame, referred here as *telescope frame*.

Let $\hat{i}_{bf}, \hat{j}_{bf}, \hat{k}_{bf}$ be the unit vectors corresponding to the Cartesian axes x_{bf}, y_{bf}, z_{bf} of the *beam frame*; \hat{k}_{bf} defines the direction of the beam centre axis in the *telescope frame*. The *beam frame* is defined with respect to the *telescope frame* by three angles: θ_B, ϕ_B, ψ_B (θ_B and ϕ_B , two standard polar coordinates defining the direction of the beam centre axis, range respectively from 0° , for an on-axis beam, to some degrees, for LFI off-axis beams, and from 0° to 360°).

Let $\hat{i}'_{bf}, \hat{j}'_{bf}, \hat{k}'_{bf}$ ($\hat{k}'_{bf} = \hat{k}_{bf}$) be the unit vectors corresponding to the Cartesian axes x', y', z' of an *intermediate frame*, defined by the two angles θ_B and ϕ_B , obtained by the *telescope frame* x, y, z when the unit vector of the axis z is rotated by an angle θ_B on the plane defined by the unit vector of the axis z and the unit vector \hat{k}_{bf} up to reach \hat{k}_{bf} :

$$\hat{k}'_{bf} = \hat{k}_{bf} = \cos(\phi_B)\sin(\theta_B)\hat{i} + \sin(\phi_B)\sin(\theta_B)\hat{j} + \cos(\theta_B)\hat{k} \quad (\text{A.1})$$

$$\hat{i}'_{bf} = [\cos(\phi_B)^2\cos(\theta_B) + \sin(\phi_B)^2]\hat{i} + [\sin(\phi_B)\cos(\phi_B)(\cos(\theta_B) - 1)]\hat{j} - \sin(\theta_B)\cos(\phi_B)\hat{k} \quad (\text{A.2})$$

$$\hat{j}'_{bf} = [\sin(\phi_B)\cos(\phi_B)(\cos(\theta_B) - 1)]\hat{i} + [\cos(\theta_B)\sin(\phi_B)^2 + \cos(\phi_B)^2]\hat{j} - \sin(\theta_B)\sin(\phi_B)\hat{k} \quad (\text{A.3})$$

The *beam frame* is obtained from the *intermediate frame* through a further (anti-clockwise) rotation of an angle ψ_B (ranging from 0° to 360° ⁷) around \hat{k}_{bf} and is therefore explicitly given by:

⁷ We note that, in other conventions, angles ϕ'_B and ψ'_B ranging from -180° to 180° are given, instead of ϕ_B and ψ_B . The angles ϕ_B and ψ_B here defined are equal to ϕ'_B and ψ'_B when they are positive and are given respectively by $360^\circ + \phi'_B$ and $360^\circ + \psi'_B$ for negative ϕ'_B and ψ'_B .

$$\begin{aligned} \hat{i}_{bf} = & [\cos(\psi_B)\hat{i}'_{bf,x} + \sin(\psi_B)\hat{j}'_{bf,x}]\hat{i} + [\cos(\psi_B)\hat{i}'_{bf,y} + \sin(\psi_B)\hat{j}'_{bf,y}]\hat{j} \\ & + [\cos(\psi_B)\hat{i}'_{bf,z} + \sin(\psi_B)\hat{j}'_{bf,z}]\hat{z}, \end{aligned} \quad (\text{A.4})$$

$$\begin{aligned} \hat{j}_{bf} = & [-\sin(\psi_B)\hat{i}'_{bf,x} + \cos(\psi_B)\hat{j}'_{bf,x}]\hat{i} + [-\sin(\psi_B)\hat{i}'_{bf,y} + \cos(\psi_B)\hat{j}'_{bf,y}]\hat{j} \\ & + [-\sin(\psi_B)\hat{i}'_{bf,z} + \cos(\psi_B)\hat{j}'_{bf,z}]\hat{z}, \end{aligned} \quad (\text{A.5})$$

where the bottom index x (y, z) indicates the component of *intermediate frame* unit vector along the axis x (y, z) of the *telescope frame*, as defined by eqs. (A1–A3).

Appendix B: Simulations at 30 GHz

The feed horn at 30 GHz considered in these simulations is specified by its Spherical Wave Expansion (SWE) provided by Alcatel Space Industries, since the sub reflector is in the near field of the corrugated horn and near field effects cannot be neglected. The feed horn directivity is about 22 dBi, the ET is 30 dB at 22° , and the main beam has a FWHM resolution of $33.73'$. The beam position and orientation is identified by $(\theta_B, \phi_B, \psi_B) = (4.3466^\circ, 153.6074^\circ, 337.5^\circ)$.

We carry out the simulation of PLANCK observation as described in Sect. 2 by assuming both the Galactic templates presented in Sect. 2.2 and the WMAP map at 33 GHz. The results are summarized in Table 7 while Fig. B.1 reports the TOD corresponding to the overall straylight signal (from the far sidelobes plus intermediate pattern) for the sum of the three Galactic components described in Sect. 2.2 and for the WMAP map. In spite of the differences in the foreground templates (the dominant signal deriving from Galactic diffuse free-free emission by using the templates of Sect. 2.2 and, according to Bennett et al. 2003b, from Galactic diffuse synchrotron emission by using the WMAP map) the peak-to-peak values is at a level of $\simeq 5 - 7\mu\text{K}$ for the contributions from both the far sidelobes and the intermediate pattern (RMS $\sim 1\mu\text{K}$, mainly due to the signal in the far sidelobes). Right panel of Fig. B.1 reports shows the difference between the TOD obtained by using these two different templates: only for $\simeq 0.01\%$ (0.09, 0.3, 10 %) of the samples of the TOD the difference is larger than $4\mu\text{K}$ (3, 2, $1\mu\text{K}$). The figure shows also that differences larger than $\simeq 1 - 2\mu\text{K}$ are localized quite close to the Galactic plane, where the CMB anisotropy is dominated by the very high Galactic signal in the main beam. This implies that a subtraction of the GSC well down to $\sim 1\mu\text{K}$ level does not require a particularly accurate description of the microwave sky emission nor particularly sophisticated computations, even at frequencies where the GSC is relevant, but it is mainly related to a good knowledge of the antenna pattern response.

Clearly, the unsubtracted GSC is relevant at frequencies far from the “cosmological window”. On the other hand, this results represent a significant optical improvement

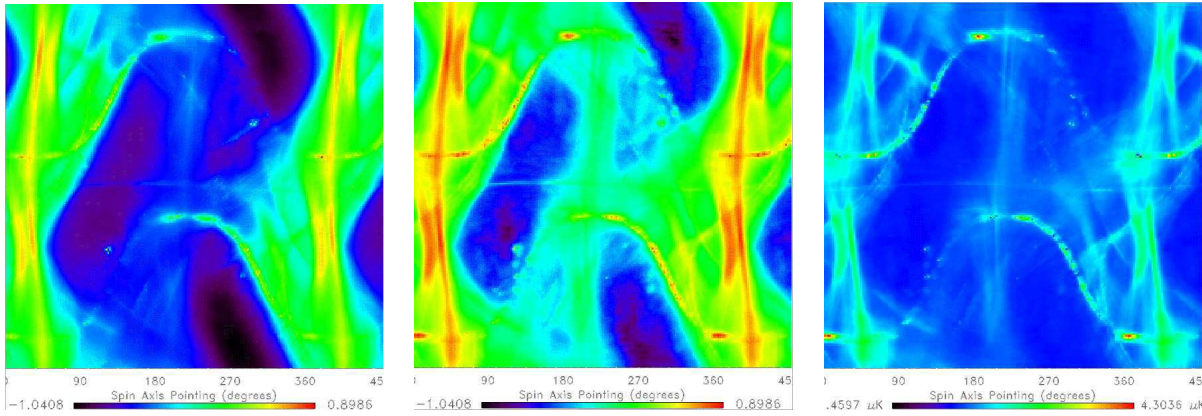


Fig. B.1. The same as in Fig. 4, but for the simulation at 30 GHz and the overall straylight signal. For a better comparison the adopted temperature range is the same in the two panels, although the minimum and maximum values are just different, as evident from the different peak-to-peak values reported in Table B.1. The right panel reports (antenna temperature in linear, not logarithm, scale, in this case) the difference between the middle panel and the left panel (see also the text).

compared to the analyses of GSC at 30 GHz by Burigana et al. (2001), based on the optical simulations by De Maagt et al. (1998), predicting a similar level of GSC from the far sidelobes but a contamination from the intermediate pattern significantly worse (peak-to-peak of about $15\mu\text{K}$). This reduction of GSC from the intermediate pattern is due to the corresponding contribution to the integrated response from the antenna pattern at few degrees from the beam centre direction, significantly reduced in the actual optimized optical design ⁸.

References

- Arnaud, J.V., Aliaga, A.M., Saez, D., 2002, A&A, in press
- Barnes, C., Hill, R.S., Hinshaw, G. et al. 2003, ApJ, submitted, astro-ph/0302215
- Bennett, C.L., Banday, A.J., Górski, K.M. et al. 1996a, ApJL, 464, 1
- Bennett, C.L., Halpern, M., Hinshaw, G. et al. 2003a, ApJ, submitted, astro-ph/0302207
- Bennett, C.L., Hill, R.S., Hinshaw, G. et al. 2003b, ApJ, submitted, astro-ph/0302208
- Bernard, J.P., Puget, J.L., Sygnet, J.F., Lamarre, J.M., 2002, Draft note on HFI's view on Planck Scanning Strategy, Technical Note PL-HFI-IAS-TN-SCAN01, 0.2.1
- Bersanelli, M. et al. 1996, ESA, COBRAS/SAMBA Report on the Phase A Study, D/SCI(96)3
- Bersanelli, M., Maino, D., Mennella, A., 2002, Riv. Nuovo Cimento, Vol. 25, serie 4, n. 9
- Burigana, C., Malaspina, M., Mandolesi, N. et al. 1997, Int. Rep. TeSRE/CNR 198/1997, November, astro-ph/9906360
- Burigana, C., Maino, D., Mandolesi, N. et al. 1998, A&AS, 130, 551

⁸ In fact, the (per cent) fractional contribution, $f\%$, is now $\simeq 0.045$ (0.39) for the intermediate pattern (far sidelobes), while it were about 0.6 (1) for the intermediate pattern (far sidelobes) in the case of the previous analysis.

Table B.1. The same as in Table 1, but for the beam pattern simulated at 30 GHz. We report also the result based on the WMAP map at 33 GHz, including all components.

LFI27 SWE						
BEAM					SKEWNESS	KURTOSIS
REGION	AVERAGE	VARIANCE	RMS	PEAK-TO-PEAK	INDEX	INDEX
DUST + DIFFUSE FREE-FREE EMISSION						
I12	3.13×10^{-2}	1.15×10^{-2}	1.07×10^{-1}	$2.72 \times 10^{+0}$	$9.45 \times 10^{+0}$	$1.21 \times 10^{+2}$
F12	4.75×10^{-1}	2.62×10^{-1}	5.12×10^{-1}	$3.09 \times 10^{+0}$	$1.64 \times 10^{+0}$	$2.32 \times 10^{+0}$
I + F	5.07×10^{-1}	2.71×10^{-1}	5.20×10^{-1}	$3.09 \times 10^{+0}$	$1.53 \times 10^{+0}$	$1.90 \times 10^{+0}$
DIFFUSE SYNCHROTRON EMISSION						
I12	2.97×10^{-2}	2.16×10^{-3}	4.64×10^{-2}	7.22×10^{-1}	$6.72 \times 10^{+0}$	$5.89 \times 10^{+1}$
F12	4.26×10^{-1}	9.94×10^{-2}	3.15×10^{-1}	$1.47 \times 10^{+0}$	$1.27 \times 10^{+0}$	7.35×10^{-1}
I + F	4.56×10^{-1}	1.01×10^{-1}	3.17×10^{-1}	$1.46 \times 10^{+0}$	$1.18 \times 10^{+0}$	4.90×10^{-1}
HII REGIONS						
I12	4.33×10^{-3}	2.54×10^{-3}	5.04×10^{-2}	$4.65 \times 10^{+0}$	$4.27 \times 10^{+1}$	$2.91 \times 10^{+3}$
F12	5.79×10^{-2}	5.78×10^{-3}	7.60×10^{-2}	7.61×10^{-1}	$1.80 \times 10^{+0}$	$3.73 \times 10^{+0}$
I + F	6.23×10^{-2}	8.40×10^{-3}	9.17×10^{-2}	$4.84 \times 10^{+0}$	$8.41 \times 10^{+0}$	$2.84 \times 10^{+2}$
SUM OF THE ABOVE COMPONENTS						
I12	6.54×10^{-2}	3.18×10^{-2}	1.78×10^{-1}	$5.34 \times 10^{+0}$	$9.35 \times 10^{+0}$	$1.25 \times 10^{+2}$
F12	9.60×10^{-1}	8.02×10^{-1}	8.96×10^{-1}	$5.05 \times 10^{+0}$	$1.51 \times 10^{+0}$	$1.74 \times 10^{+0}$
I + F	$1.03 \times 10^{+0}$	8.28×10^{-1}	9.10×10^{-1}	$7.77 \times 10^{+0}$	$1.42 \times 10^{+0}$	$1.46 \times 10^{+0}$
WMAP AT 33 GHz						
I12	1.10×10^{-1}	1.05×10^{-1}	3.24×10^{-1}	$6.17 \times 10^{+0}$	$7.75 \times 10^{+0}$	$7.72 \times 10^{+1}$
F12	$1.37 \times 10^{+0}$	$1.51 \times 10^{+0}$	$1.23 \times 10^{+0}$	$6.76 \times 10^{+0}$	$1.40 \times 10^{+0}$	$1.45 \times 10^{+0}$
I + F	$1.48 \times 10^{+0}$	$1.61 \times 10^{+0}$	$1.27 \times 10^{+0}$	$7.18 \times 10^{+0}$	$1.29 \times 10^{+0}$	$1.07 \times 10^{+0}$

Burigana, C., Maino, D., Natoli, P. et al. 2000, Straylight effects and beam reconstruction in Planck/LFI observations, talk at the “Planck Scanning Strategy Meeting”, Villa Mondragone - Monteporzio Catone (Roma), Italy, 22-23 June 2000

Burigana, C., Maino, D., Görski, K.M. et al. 2001, A&A, 373, 345

Burigana, C., Natoli, P., Vittorio, N., Mandolesi, N., Bersanelli, M., 2002, Exp. Astron., 12/2, 87, 2001

Challinor, A., Fosalba, P., Mortlock, D. et al. 2000, Phys. Rev. D, 65, 023505

De Maagt, P., Polegre, A.M., Crone, G., 1998, PLANCK – Straylight Evaluation of the Carrier Configuration, Technical Report ESA, PT-TN-05967, 1/0

De Zotti, G., Toffolatti, L., Argüeso Gómez, F. et al. 1999, Proceedings of the EC-TMR Conference “3 K Cosmology”, Roma, Italy, 5-10 October 1998, AIP Conference Proc. 476, Maiani L., Melchiorri F., Vittorio N., (Eds.), pg. 204, astro-ph/9902103

Dubruel, D., Cornut, M., Fargant, G. et al. 2000, in “Millennium Conference on Antennas & Propagation - 2000”, Danesy D. & Sawaya H., (Eds.), ESA Conference Proceedings SP-444, European Space Agency, CD-ROM

Please give a shorter version with: \authorrunning and/or \titilerunning prior to \maketitle

- Giardino, G., Banday, A.J., Górski, K.M. et al. 2002, A&A, 387, 82
- Górski, K.M., Hivon, E., Wandelt, B.D., 1999, “Proceedings of the MPA/ESO Conference on Evolution of Large-Scale Structure: from Recombination to Garching”, ed. Banday A.J., Sheth R.K., Da Costa L., pg. 37, astro-ph/9812350
- Haslam, C.G.T. et al. 1982, A&AS, 47, 1
- Hinshaw, G., Barnes C., Bennett, C.L. et al. 2003a, ApJ, submitted, astro-ph/0302222
- Hinshaw, G., Spergel, D.N., Verde, L. et al. 2003b, ApJ, submitted, astro-ph/0302217
- Kogut, A., Spergel, D.N., Barnes, C. et al. 2003, ApJ, submitted, astro-ph/0302213
- Lamarre, J.M., Maffei, B., Ade, P.A.R. et al. 2002, in “Experimental Cosmology at millimetre wavelengths – 2K1BC Workshop”, Breuil-Cervinia (AO), Valle d’Aosta, Italy, 9-13 July 2001, AIP Conference Proc. 616, De Petris M., Gervasi M., (Eds.), pg. 213
- Maino, D., Burigana, C., Maltoni, M. et al. 1999, A&AS, 140, 383
- Maino, D., Farusi, A., Baccigalupi, C. et al. 2002, MNRAS, 334, 53
- Mandolesi, N. et al. 1998, PLANCK LFI, A Proposal Submitted to the ESA
- Mandolesi, N., Bersanelli, M., Burigana, C., Villa, F., 2000a, Astroph. Lett. Comm., 37, 151
- Mandolesi, N., Bersanelli, M., Burigana, C. et al. 2000b, A&AS, 145, 323
- Mandolesi, N., Bersanelli, M., Butler, R.C. et al. 2002, in “Experimental Cosmology at millimetre wavelengths – 2K1BC Workshop”, Breuil-Cervinia (AO), Valle d’Aosta, Italy, 9-13 July 2001, AIP Conference Proc. 616, De Petris M., Gervasi M., (Eds.), pg. 193
- Netterfield, C.B., Ade, P.A.R., Bock, J.J. et al. 2002, ApJ, 571, 604
- Page, L., Barnes, C., Hinshaw, G. et al. 2003, ApJ, submitted, astro-ph/0302214
- Paladini, R., Burigana, C., Davies, R.D. et al. 2003, A&A, 397, 213
- Pryke, C., Halverson, N.W., Leitch, E.M. et al. 2002, ApJ, 568, 46
- Puget, J.L. et al. 1998, HFI for the PLANCK Mission, A Proposal Submitted to the ESA
- Sandri, M., Villa, F., Nesti, R. et al. 2003, A&A, to be submitted (Paper I)
- Schlegel, D.J., Finkbeiner, D.P., Davies, M., 1998, ApJ, 500, 525
- Spergel, D.N., Verde, L., Peiris, H.V. et al. 2003, ApJ, submitted, astro-ph/0302209
- Stompor, R., Abroe, M., Ade, P. et al. 2001, ApJ, 561, L7
- Tauber, J. A., “The PLANCK Mission”, in *The Extragalactic Infrared Background and its Cosmological Implications*, Proceedings of the IAU Symposium, Vol. 204, 2000, M. Harwit and M. Hauser, eds.
- Villa, F., Bersanelli, M., Burigana, C. et al. 2002, in “Experimental Cosmology at millimetre wavelengths – 2K1BC Workshop”, Breuil-Cervinia (AO), Valle d’Aosta, Italy, 9-13 July 2001, AIP Conference Proc. 616, De Petris M., Gervasi M., (Eds.), pg. 224, astro-ph/0112173
- Villa, F., Mandolesi, N., Burigana, C., 1998, Int. Rep. TeSRE/CNR 221/1998, September
- Villa, F., Mandolesi, N., Butler, R.C., 2003, “The PLANCK Project”, Mem. S.A.it, Vol. 74, 223